Original Research

Boosting Biocatalytic Redox Cycles: One-Step B–Se Co-doped g-C_3N_4/Eosin B for Solar 1,4-NADH Recycling

Surya Pratap Singh [1], Rajesh K. Yadav [1,*], Shaifali Mishra [1], Rehana Shahin [1,3], Kanchan Sharma [1], Surendra K. Jaiswal [1], Anupma Yadav [1], Geeta Srivastava [1], Anurag Rai [1], Vinay K. Mishra [1], Anushka Pandey [1], Rahul Maddeshiya [1], Pragya Singh [1], D. K. Dwivedi [2,*]

[1] Department of Chemistry and Environmental Science, Madan Mohan Malaviya University of Technology, Gorakhpur-273010, U.P., India,

[2] Department of Physics and Material Science, Madan Mohan Malaviya University of Technology, Gorakhpur-273010, U.P., India

[3] Department of Physical Sciences Starex University Delhi-NCR Gurugram

*Correspondence: rajeshkr_yadav2003@yahoo.co.in

Received: February 18, 2026; Accepted: June 9, 2026

Abstract: The efficient and selective regeneration of nicotinamide adenine dinucleotide (NADH) remains a significant challenge in biocatalysis due to the limited availability of sustainable and metal-free photocatalytic systems. Herein, we report a novel metal-free photocatalytic strategy that integrates boron- and selenium-doped graphitic carbon nitride (B–Se–g-C_3N_4) with Eosin B (EB) as a synergistic photosensitizer for highly selective NADH regeneration. The novelty lies in the rational combination of heteroatom co-doping (B and Se) with an organic dye to enhance charge separation and selectively promote 1,4-NADH under irradiation. The developed system exhibits a high photo-regeneration efficiency of 95.83% with excellent selectivity toward the biologically active 1,4-NADH isomer. This approach not only expands the scope of dye-assisted, metal-free photocatalysis but also establishes a sustainable and efficient platform for cofactor regeneration, advancing green chemistry and biocatalytic applications.

Keywords: visible light, EB, B-Se-g-C_3N_4, EB-B-Se-g-C_3N_4, biomaterial (1,4-NADH), amide bond

1. Introduction

Photosynthesis is a process by which photoautotrophs store energy in chemical bonds. It is a most significant biological process on Earth that fixes atmospheric carbon dioxide (CO_2), thereby serving as a natural energy source for living organisms [1,2]. In this context, an artificial photocatalytic pathway was constructed to satisfy the extraordinary challenges of the chemical society. In biochemical society, the cofactor cycling to reduced nicotinamide adenine dinucleotide (NADH) has a significant role in assisting redox reactions involving oxidoreductase enzymes [3–5]. The in-situ photo-regeneration of NADH is crucial due to the optimal quantity of NADH-dependent enzymes required in the biocatalytic procedure [6,7]. Previous studies have reported that the three NADH-dependent enzymes were used to fix atmospheric CO_2 into respective useful fuels, i.e. hydrogenases like formate, formaldehyde, and alcohol [8,9]. While enzymatic conversion of CO_2 into biofuel is environmentally beneficial, the high cost of NADH makes the process unrealistic, highlighting the need for an efficient regeneration system [10].

Visible-light-driven 1,4-NADH regeneration has emerged as a green and energy-efficient strategy for sustaining biocatalytic redox cycles. In artificial photosynthesis, coupling photocatalysts with enzymatic

systems enables efficient solar-to-chemical energy conversion, where continuous NADH regeneration is crucial for driving downstream transformations [11,12]. Among the range of photocatalysts, graphitic carbon nitride (g-C_3N_4) has gained significant interest due to its acceptable band structure, high stability, and visible-light activity. However, its realistic application is limited by poor light absorption, rapid carrier recombination, and a limited number of active sites. To overcome these limitations, heterostructure engineering and doping strategies have been widely used to modulate its electronic properties and enhance charge separation. In particular, constructing heterojunctions enhances interfacial electron transfer, while introducing transition heteroatom–nitrogen (Se/B-N) sites, creates active centres and facilitates charge delocalization [13]. Additionally, defect engineering and heteroatom incorporation further improve the visible-light absorption and charge migration efficiency.

Efficient NADH regeneration is essential for maintaining stable NAD^+/NADH cycling in enzymatic reactions. Earlier studies, including those by Galarneau and co-workers, demonstrated that integrating enzymatic regeneration systems significantly enhances product yields in multi-enzyme processes [14,15]. NADH can be regenerated via chemical [16] photochemical [17–19] enzymatic [20–22] or electrochemical routes [23,24] Among these methods, photocatalysis has gained attention due to its compatibility with solar energy [25]. In this regard, light-harvesting components such as Eosin B and g-C_3N_4 have been widely explored for solar-driven production of NADH and NADPH [26,27]. Although metal-based photocatalysts exhibit high activity, their limited response to ultraviolet light restricts practical applications [28]. However, semiconductor-based systems with engineered band structures have been developed to enhance visible-light utilization [29]. Beyond cofactor regeneration, photocatalysis has also shown strong potential in green organic transformations, including C(sp^3)–O bond activation, due to its efficiency and environmentally benign nature [30].

Despite these advances, achieving highly selective and efficient 1,4-NADH regeneration remains a significant challenge due to limited control over charge transfer pathways and product selectivity. In the present study, we introduce a novel strategy built on the synergistic integration of boron and selenium co-doping in g-C_3N_4 with Eosin B as an organic photosensitizer. The novelty of this work lies in (i) the rational design of a dual-modified photocatalytic system combining heteroatom co-doping and dye sensitization, (ii) the enhancement of visible-light absorption and charge carrier separation, and (iii) the achievement of highly selective 1,4-NADH regeneration with superior efficiency.

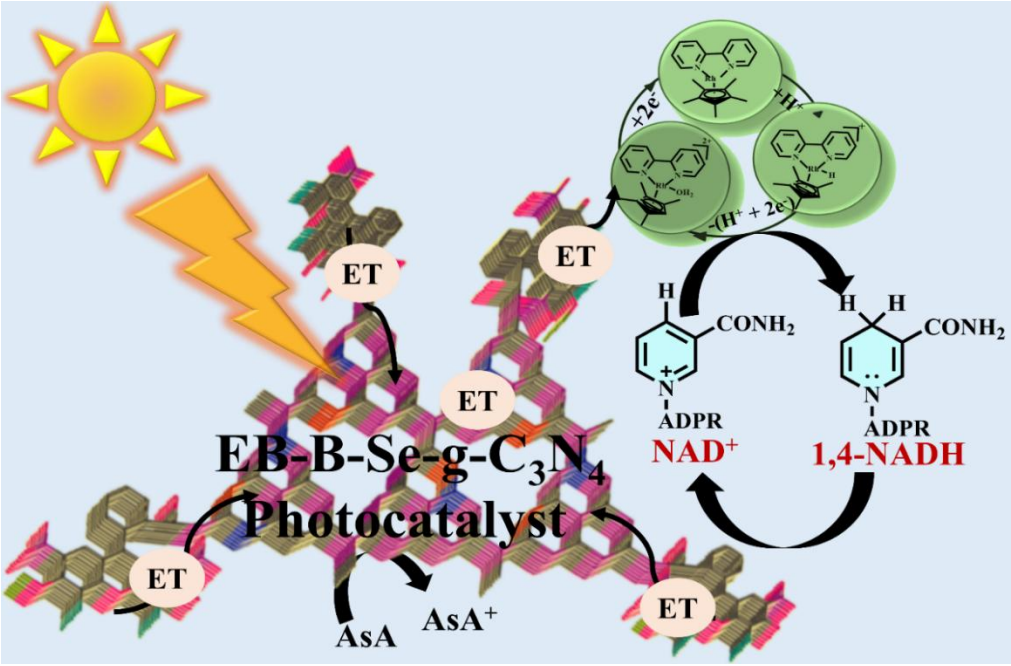

Scheme 1. An artificial photosynthetic pathway showing photo-regeneration of 1,4-NADH.

2. Materials and methods

The materials were purchased from TCI India, BLD Pharma, and Sigma Aldrich. Boric acid (purity= 99.5%), melamine (purity= 97.5%), selenium dioxide (purity= 99.5%), Eosin-B/EB (purity= 90%), 1,2-Dichlorobenzene (ODCB) (purity= 99%), Hexafluorophosphate Azabenzotriazole tetramethyluranium (HATU) (purity= 98%), ascorbic acid (AsA) (purity= 99.7%), sodium/potassium mono/dibasic salts (extra pure) and nicotinamide adenine dinucleotide (NAD^+) co-factor (purity= 98%), N, N′ dimethylformamide (DMF) (purity= 99.5%). The phosphate buffer solution (PBS) was prepared via sodium/potassium mono/dibasic salts. Pentamethylcyclopentadienyl)Rhodium (III) dichloride dimer (purity= 96%) was ultilized for preparing rhodium complex (Rh-C). Deionised water was used throughout the experiment.

A Shimadzu UV-1900 and 800 IR sprit spectrophotometer was used to obtain absorption and infrared spectra. A CH1608E, 220 V instrument was used for analyzing electrochemical characterizations. However, PXRD and morphological analysis were performed via D8 Advance Eco diffractometer and JEOL SEM IT 300, respectively.

2.1. Synthesis of B-Se-g-C_3N_4

Synthesis of B-Se-g-C_3N_4 followed the standard method [31]. 500 mg of boric acid, 500 mg of selenium dioxide, and 1g of melamine were allowed to be mixed in distilled water. The dissolved mixture was subsequently evaporated at 100°C using a magnetic stirrer. The obtained white precipitate was dried and kept in the ceramic-based crucible, which was further calcined at 500°C with a heating rate of 5 °C/min for 4 hrs. The obtained yellow-coloured crude product was subsequently washed for characteriations and applications, Scheme 2.

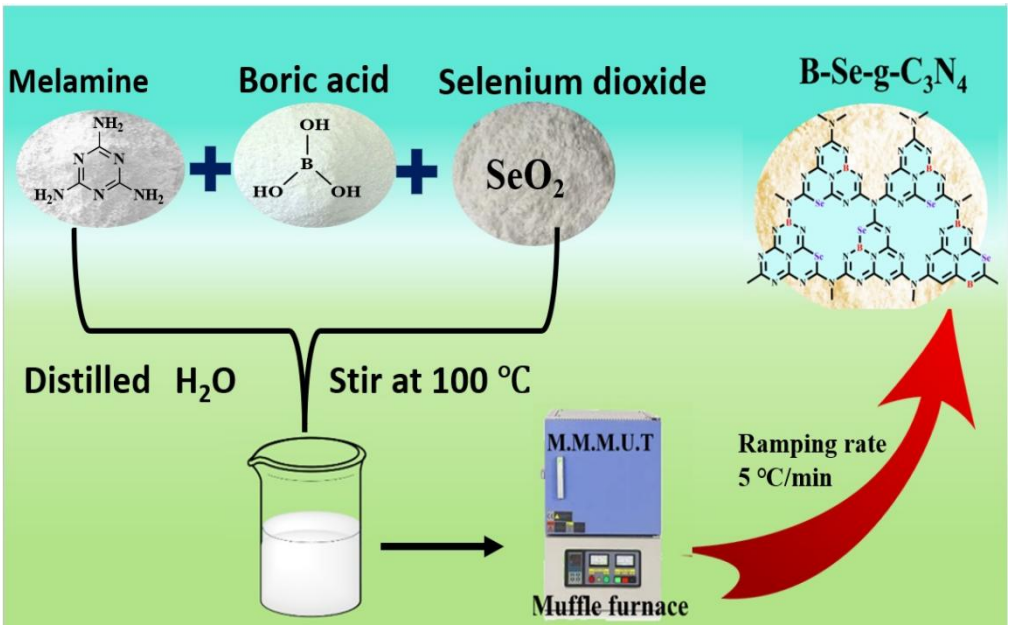

Scheme 2. Schematic representation of grafting B-Se-g-C_3N_4.

2.2. Synthesis of EB-B-Se-g-C_3N_4 photocatalyst

The EB-B-Se-g-C_3N_4 photocatalyst was demonstrated through a polycondensation mechanism [32]. 300 mg of B-Se-g-C_3N_4, 500 mg of EB, 10 mL ODCB, 5mL DMF, and a catalytic amount of HATU were taken in a double-necked round-bottom flask. The flask was then refluxed for 96 hours at 250 °C. After 96 hours, the red-coloured reaction mixture was filtered to obtain red-coloured precipitate, which was further washed with distilled water, Scheme 3 [33].

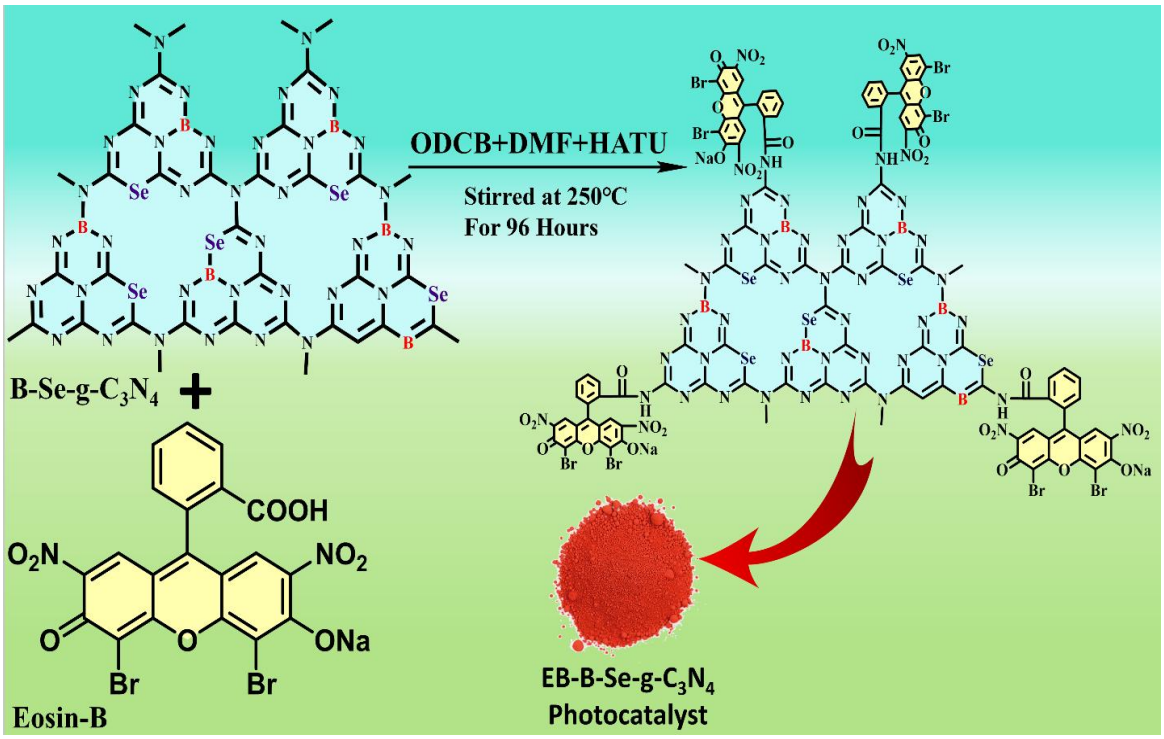

Scheme 3. Schematic representation of the synthesis of EB-B-Se-g-C_3N_4 photocatalyst.

3. Results & discussion

3.1. Photocatalytic regeneration of 1,4-NADH

The photo-regeneration of 1,4-NADH was performed via the reported literature. [9, 37] In a quartz glass vail confrigurated with, a magnetic stirrer was placed below a blue LED light. The glass vail was composed of AsA, Rh-C (prepared using the standard method) [34], NAD^+ co-factor, EB-B-Se-g-C_3N_4 photocatalyst dispersed in a PBS at pH-7. The mixture was purged with N_2 to maintain inertness. The photo-regeneration of 1,4-NADH was tracked through a spectrophotometer at regular intervals. The resultant spectra show an increment in absorbance at 340 nm at every successive interval, which implies 1,4-NADH regeneration with an excellent yield of 95.83%, implying better ability to give photocatalytic activity than their precursors [85.33 %] (Figure 1a and b) [31].

Moreover, irradiation ($\lambda \geq 420$ nm), the photocatalyst generates charge carriers, with electrons promoted to the conduction band (-3.335 V) and holes left in the valence band (-5.995 V). The photogenerated electrons are sequentially transferred from the conduction band to the Rh catalytic center (−3.96 V) and subsequently to NAD^+ (-4.20 V), facilitating its reduction to NADH. Concurrently, the valence band holes are effectively scavenged by ascorbic acid (AsA), which undergoes oxidation, thereby suppressing charge recombination and maintaining continuous electron flow. This cascade electron transfer pathway promotes efficient charge separation and enables selective photocatalytic regeneration of NADH, Scheme 4 [35].

Additionally, the reusability of the EB-B-Se-g-C_3N_4 photocatalyst was evaluated via five consecutive catalytic cycles. The photocatalyst retained its activity with negligible loss in NADH regeneration efficiency over multiple cycles, confirming its excellent structural stability and recyclability under visible-light irradiation (Figure 1c).

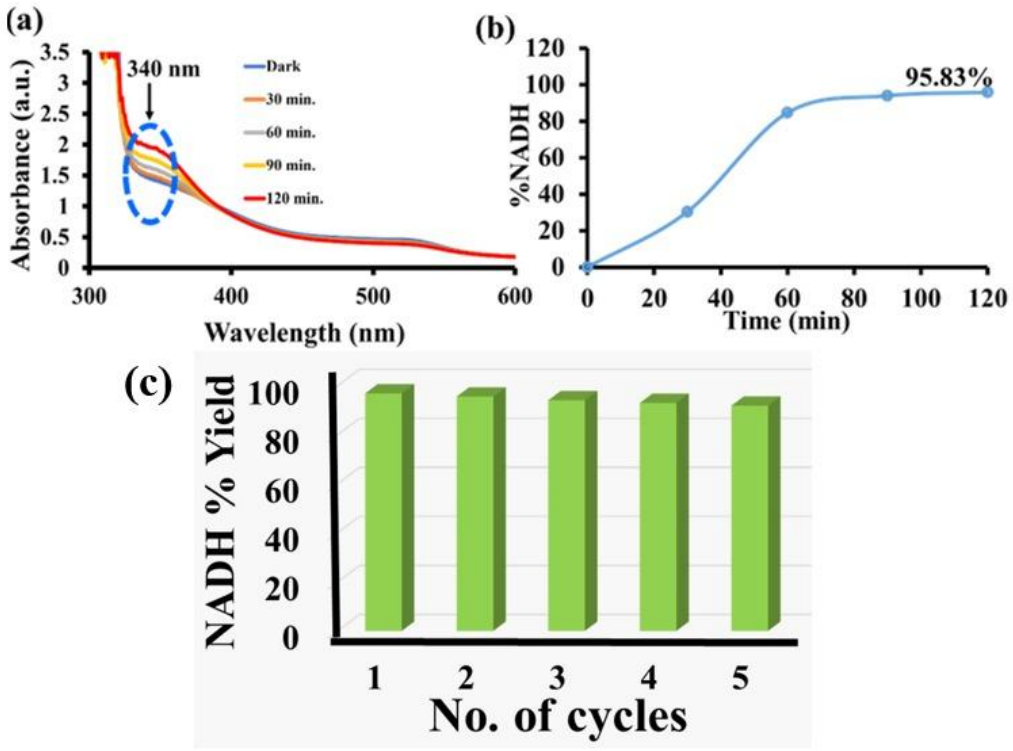

Figure 1. (a) UV-visible absorption spectra of the performed 1,4-NADH regeneration, (b) 1,4-NADH regeneration yield, and (c) Reusability result of 1,4-NADH from the EB–B-Se-g-C_3N_4 photocatalyst.

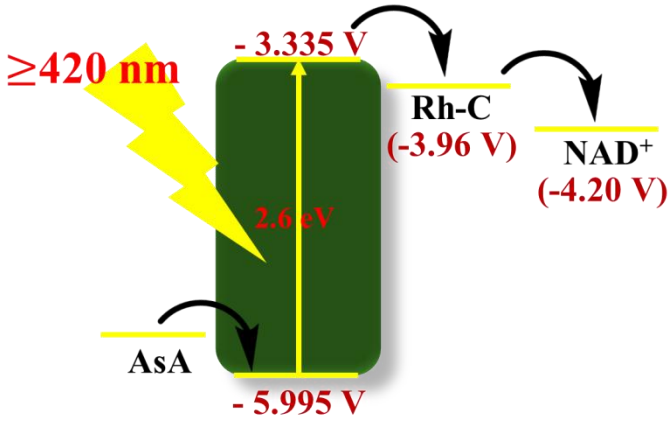

Scheme 4. Electron transfer mechanism for 1,4-NADH regeneration.

4. Discussion

4.1. UV-visible spectra & FTIR: Unlocking the secrets of molecular signatures

The electronic transitions, along with optical ability, have been studied using UV-visible spectra, which were consistent with previous literature [15,36]. The Figure 2(a) shows the absorption spectra of EB, B-Se-g-C_3N_4, and EB-B-Se-g-C_3N_4 photocatalyst. EB shows a narrower absorption band at 500-560 nm, while the B-Se-g-C_3N_4 shows no absorption in the interest area. However, the EB-B-Se-g-C_3N_4 photocatalyst shows a wider range of absorption spectra at 500-600 nm, implying the bathochromic shift (red shift). The optical band gap of EB-B-Se-g-C_3N_4 photocatalyst came to be ~ 2.29 eV by applying the Scherrer equation. In addition, the diffuse reflectance spectroscopy (DRS) also supports the wider absorption spectra of the EB-B-Se-g-C_3N_4 photocatalyst.

The Tauc plot was also calculated through DRS calculations, providing the band gap of EB-B-Se-g-C_3N_4 photocatalyst, which comes to be 2.5 eV, lying in the semiconductor region, indicating the semiconductor nature of EB-B-Se-g-C_3N_4 photocatalyst, as shown in Figure 2(b) [37]. Fourier transform infrared spectroscopy (FTIR) was used to demonstrate the group functionality and vibrational frequency through stretching vibrations. Figure 2(c) shows the EB FTIR spectra with characteristic peaks at 1561 cm^{-1}, 1750 cm^{-1}, and 3000 $cm^{-1,}$ which correspond to the stretching vibrations of phenylic group, C-O stretching of carbonyl group, and C-H stretching, respectively [38]. The FTIR spectra of g-C_3N_4 and B-Se-g-C_3N_4 depict the characteristic peaks at 1408 cm^{-1}, 1519 cm^{-1}, and 2990 cm^{-1}, corresponding to C-N, C=C, and N-H stretching vibrations, respectively [34,39]. After coupling with EB, the composite EB-B-Se-g-C_3N_4 photocatalyst shows the shifting of N-H and C=O at 3300 cm^{-1} and 1735 $cm^{-1,}$ respectively, which implies the amide bond formation between EB and B-Se-g-C_3N_4 [40].

4.2. Powdered X-ray diffraction spectroscopy: X-ray vision into crystal structures

The powder X-ray diffraction (PXRD) pattern was used to analyse crystallinity and physical changes in the moieties. The PXRD pattern of B-Se-g-C_3N_4 shows characteristic peaks at 27.13° and 13.41°corresponding to (002) and (100) planes, which are consistent with the reported literature and g-C_3N_4 core.[31,41] After coupling with EB, the resulting composite EB-B-Se-g-C_3N_4 photocatalyst shows the shifting in (002) and (100) planes, which implies the preservation of the B-Se-g-C_3N_4 moiety in the composite, Figure 2(d and e).

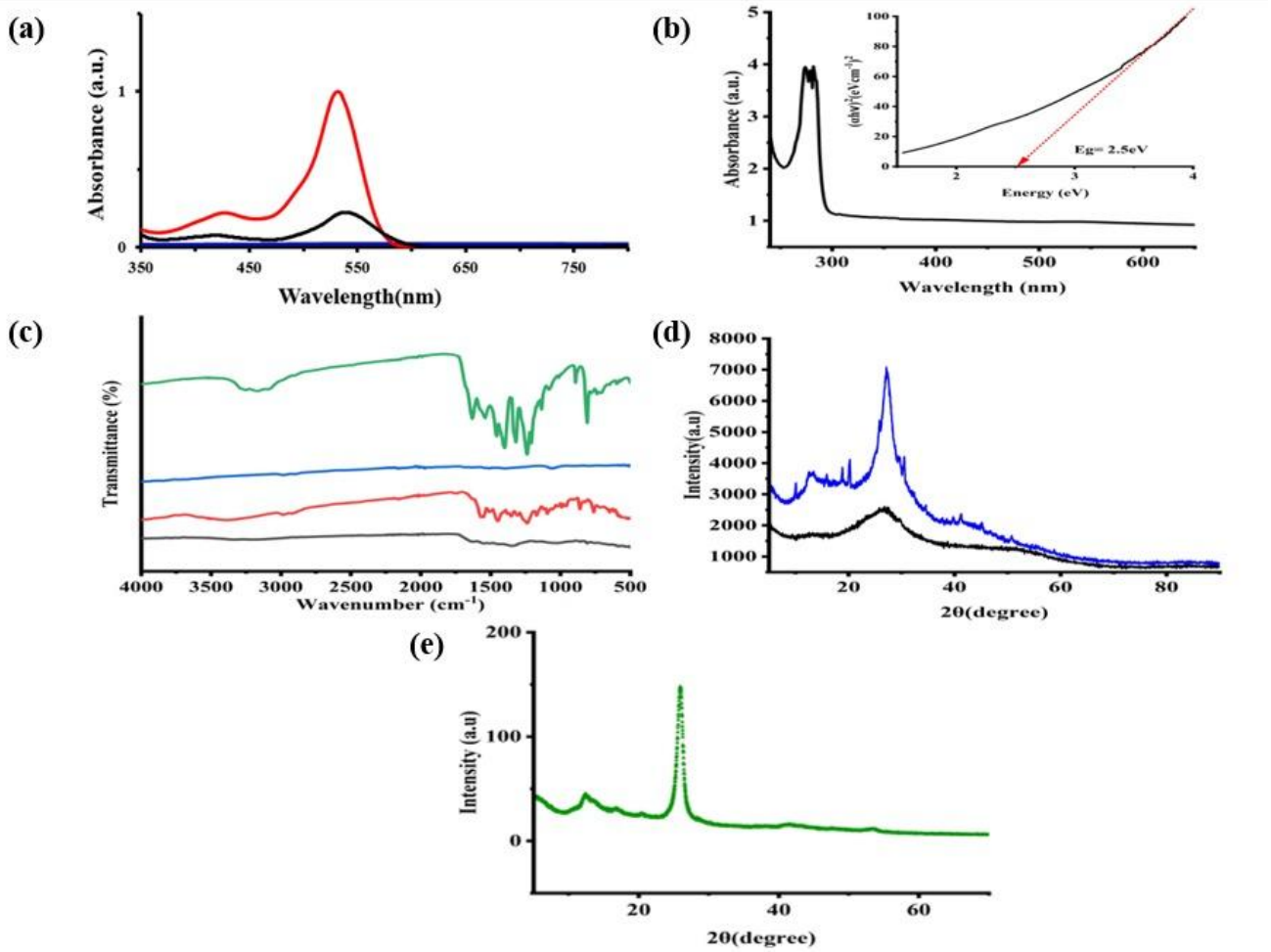

Figure 2. (a) UV–visible absorption spectra of EB (red line), EB–B-Se-g-C_3N_4 photocatalyst (black line) and B-Se-g-C_3N_4 (blue line), (b) Tauc plot of EB–B-Se-g-C_3N_4 photocatalyst to determine the optical band gap, (c) FTIR spectra of g-C_3N_4 (green), EB (red line), EB–B-Se-g-C_3N_4 photocatalyst (black line) and B-Se-g-C_3N_4 (blue line), (d) X-ray diffraction pattern of B-Se-g-C_3N_4(blue line), EB–B-Se-g-C_3N_4 photocatalyst (black line), and (e) X-ray diffraction pattern of g-C_3N_4 (green).

4.3. Electrochemical analysis: Unveiling redox secrets

The electrochemical analysis was demonstrated through a three-electrode system dipped in a 0.01 M H_2SO_4 solution using calomel as a reference electrode, glassy carbon as a working electrode, and platinum wire as a counter electrode. The cyclic voltammetry was used to analyse the redox potential of moieties as shown in Figure 3(a). The reduction and oxidation potentials of EB-B-Se-g-C_3N_4 photocatalyst are -1.165 and 1.495 V, respectively. The energy levels, HOMO/LUMO, were calculated via these redox potentials, i.e. the HOMO and LUMO levels of EB-B-Se-g-C_3N_4 photocatalyst are -5.995 V and -3.335 V, respectively. The energy band gap observed through HOMO/LUMO energy levels is 2.6 for the EB-B-Se-g-C_3N_4 photocatalyst; this energy band was also supported by the Tauc plot calculated by DRS calculations [37]. Whereas for EB and B-Se-g-C_3N_4, it is 2.8 eV and 2.7 eV, respectively [35]. Electrochemical impedance spectroscopy (EIS) was used to analyse the separation and migration of charge carriers. The Nyquist plot was used to determine the arc radius of the moieties, Figure 3(b). The lower semicircular arc radius, i.e. EB-B-Se-g-C_3N_4 photocatalyst, implies the lower resistance of the moiety, which leads to better conductivity as reported literatures [42]. However, the Tafel plot also supports the charge transfer kinetics, Figure 3(c). A lower value of slope indicates lower potential required for charge separation, implying better charge migration, which results in better photocatalytic response [43]. Chronopotentiometry is an electrochemical technique used for analysing the

current-carrying capacity of the moieties. The subsequent results are demonstrated in Figure 3(d). The results imply the photoresponse across multiple on/off cycles with respect to visible light. The better photo-response of the EB-B-Se-g-C_3N_4 photocatalyst implies the better charge transfer and separation capability of the moiety, which was harmonious with previous studies [44].

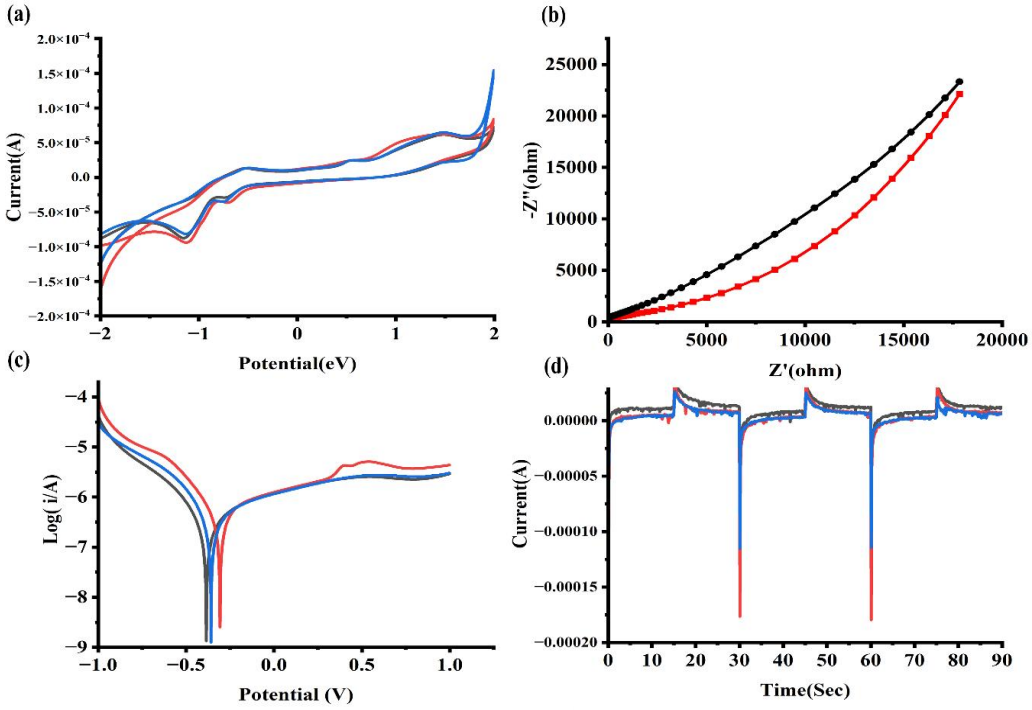

Figure 3. (a) Cyclic voltammetry of EB (red line), B-Se-g-C_3N_4 (blue line) and EB-B-Se-g-C_3N_4 photocatalyst (black line), (b) EIS of EB (red line), EB-B-Se-g-C_3N_4 (black line), (c) Tafel plot of EB (red line), B-Se-g-C_3N_4 (blue line) and EB-B-Se-g-C_3N_4 photocatalyst (black line), and (d) CP of EB (red line), B-Se-g-C_3N_4 (blue line) and EB-B-Se-g-C_3N_4 photocatalyst (black line).

4.4. Scanning electron microscopy (SEM) & Energy dispersive spectroscopy (EDS)

To explore the morphological behaviour of the moieties, scanning electron microscopy (SEM) was used. The morphology of the B-Se-g-C_3N_4 was observed to be cloth-like, while the morphology of the EB-B-Se-g-C_3N_4 photocatalyst was observed as a white, rock-like material. This change in morphology implies the EB-B-Se-g-C_3N_4 photocatalyst formation. Additionally, the occurrence of B, C, N, O, Na, Se and Br also signifies the coupling of EB and B-Se-g-C_3N_4, which was confirms by energy dispersive elemental mapping and x-ray spectroscopy, Figure 4 [36,45].

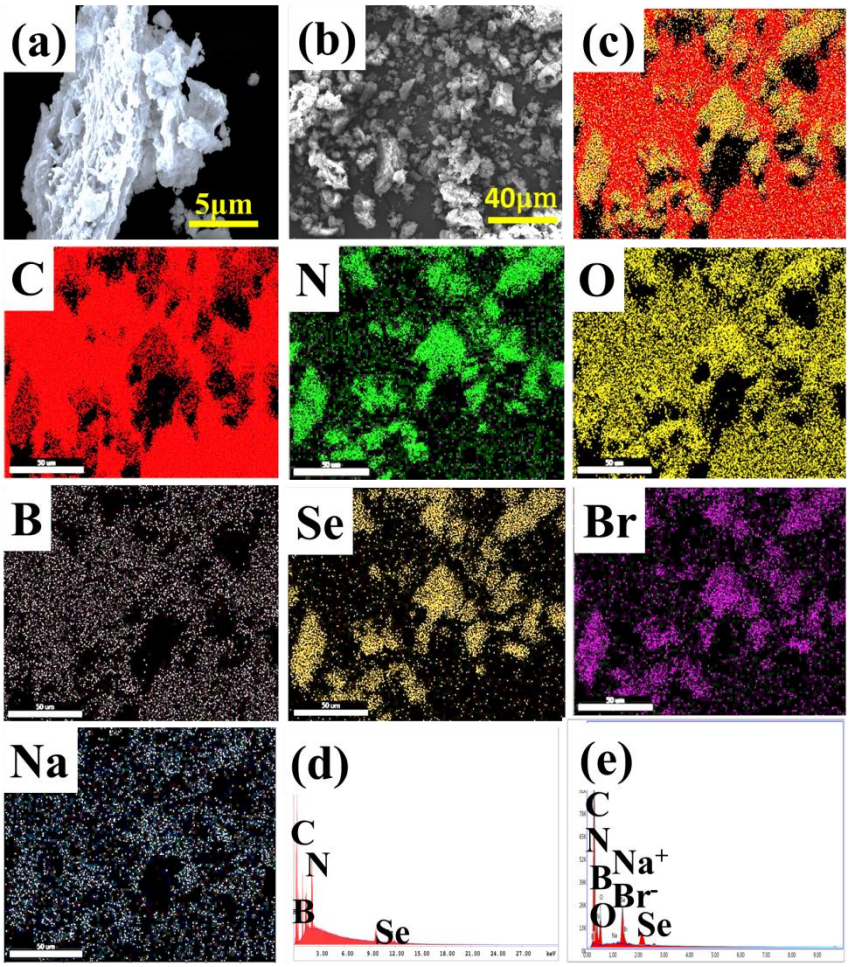

Figure 4. SEM micrographs of (a) EB-B-Se-g-C_3N_4 photocatalyst and (b) B-Se-g-C_3N_4, along with overlapped image of EB-B-Se-g-C_3N_4 photocatalyst showing carbon (red), nitrogen (green), oxygen (yellow), boron (light pink), selenium (dark yellow), bromine (pink), sodium (blue), and EDS spectra of (d) B-Se-g-C_3N_4 and (e) EB-B-Se-g-C_3N_4 photocatalyst.

5. Conclusions

In summary, we successfully synthesized an EB-B-Se-g-C_3N_4 photocatalyst via polycondensation, leading to the formation of amide bonds. The resulting EB-B-Se-g-C_3N_4 photocatalyst exhibits remarkable visible-light absorption (λ > 420 nm), enabling superior photocatalytic performance. Notably, it demonstrates an exceptional efficiency in the photocatalytic response up to 95.83%. Additionally, the EB-B-Se-g-C_3N_4 photocatalyst possesses key structural and electronic properties, contributing to its outstanding activity and stability. These findings highlight the potential of the EB-B-Se-g-C_3N_4 photocatalyst as a notably efficient photocatalyst for advanced photocatalytic regeneration under irradiation.

Availability of Data and Materials: The data supporting the findings of this study can be obtained upon request from the corresponding author. They are not publicly accessible due to privacy or ethical constraints.

Author Contributions: Surya Pratap Singh drafted the original manuscript and developed the methodology. Rajesh K. Yadav supervised the project and validated the findings. Shaifali Mishra, Rehana Shahin, Kanchan Sharma, Anurag Rai, and Anushka Pandey performed formal analysis. Surendra K. Jaiswal, Anupma Yadav, Rahul Maddeshiya, and Pragya Singh carried out data curation. Geeta Srivastava conducted data analysis. Vinay K. Mishra edited the manuscript. D. K. Dwivedi reviewed the manuscript and contributed to validation. All authors contributed to editorial changes in the manuscript. All authors have read and approved the final manuscript. All authors have participated sufficiently in the

work and agree to be accountable for all aspects of the work.

Acknowledgment: We sincerely thank Madan Mohan Malaviya University of Technology, Gorakhpur, for the research work.

Funding: This research received no external funding.

Conflict of Interest: The authors declare that they have no known competing financial interests or personal relationships that could have appeared to influence the work reported in this paper.

Declaration of AI and AI-assisted Technologies in the Writing Process: No AI or AI-assisted technologies were used in the preparation of this manuscript. The work has been verified through plagiarism screening, and the AI similarity index is 0% as confirmed by Turnitin.

References

1. Hou, H. J. M.; Najafpour, M. M.; Moore, G. F.; Allakhverdiev, S. I. *Photosynthesis: Structures, mechanisms, and applications*; Springer, 2017; Vol. 417. https://doi.org/10.1007/978-3-319-48873-8

2. Mata, T. M.; Martins, A. A.; Caetano, N. S. Microalgae for biodiesel production and other applications: A review. *Renewable and Sustainable Energy Reviews* 2010, *14*(1), 217–232. https://doi.org/10.1016/j.rser.2009.07.020

3. Chaubey, S.; Yadav, R. K.; Kim, T. W.; Yadav, T. C.; Kumar, A.; Dwivedi, D. K.; Pandey, B. K.; Singh, A. P. Fabrication of graphitic carbon nitride-based film: An emerged highly efficient catalyst for direct C—H arylation under solar light. *Chinese Journal of Chemistry* 2021, *39*(3), 633–639. https://doi.org/10.1002/cjoc.202000470

4. Wang, Y.; Zhang, J.; Wang, X.; Antonietti, M.; Li, H. Boron-and fluorine-containing mesoporous carbon nitride polymers: Metal-free catalysts for cyclohexane oxidation. *Angewandte Chemie International Edition* 2010, *49*(19), 3356–3359. https://doi.org/10.1002/anie.201000120

5. Su, F.; Mathew, S. C.; Lipner, G.; Fu, X.; Antonietti, M.; Blechert, S.; Wang, X. Mpg-C_3N_4-catalyzed selective oxidation of alcohols using O_2 and visible light. *Journal of the American Chemical Society* 2010, *132*(46), 16299–16301. https://doi.org/10.1021/ja102866p

6. Jayakumar, K.; Fera, M.-C.; Abad, J. M.; De Lacey, A. L.; Pita, M. Efficient bioelectrocatalytic NADH regeneration with a novel amino-functionalized viologen redox polymer. *Bioelectrochemistry* 2025, *162*, 108850. https://doi.org/10.1016/j.bioelechem.2024.108850

7. Meng, J.; Tian, Y.; Li, C.; Lin, X.; Wang, Z.; Sun, L.; Zhou, Y.; Li, J.; Yang, N.; Zong, Y.; others. A thiophene-modified doubleshell hollow g-C_3N_4 nanosphere boosts NADH regeneration via synergistic enhancement of charge excitation and separation. *Catalysis Science & Technology* 2019, *9*(8), 1911–1921. https://doi.org/10.1039/C9CY00180H

8. Ahmad Rizal Lim, F. N.; Marpani, F.; Anak Dilol, V. E.; Mohamad Pauzi, S.; Othman, N. H.; Alias, N. H.; Nik Him, N. R.; Luo, J.; Abd Rahman, N. A review on the design and performance of enzyme-aided catalysis of carbon dioxide in membrane, electrochemical cell and photocatalytic reactors. *Membranes (Basel)* 2021, *12*(1), 28. https://doi.org/10.3390/membranes12010028

9. Saba, T.; Burnett, J. W. H.; Li, J.; Kechagiopoulos, P. N.; Wang, X. A facile analytical method for reliable selectivity examination in cofactor NADH regeneration. *Chemical Communications* 2020, *56*(8), 1231–1234. https://doi.org/10.1039/C9CC07805C

10. Long, N. V. D.; Lee, J.; Koo, K.-K.; Luis, P.; Lee, M. Recent progress and novel applications in enzymatic conversion of carbon dioxide. *Energies* 2017, *10*(4), 473. https://doi.org/10.3390/en10040473

11. Guo, P.; Xue, R.; Zou, Q.; Ma, X.; Su, C.; Zeng, Z.; Li, L. Enhanced ultramicropore of biomass-derived porous carbon for efficient and low-energy CO_2 capture: Integration of adsorption and solar desorption. *Energy & Environmental Materials* 2026, *9*(2), e70140. https://doi.org/10.1002/eem2.70140

12. Zhao, M.; Huang, J.; Yang, H.; Yang, R.; Guo, S.; Liu, Z.; Xie, Q.; Li, M.; Fan, Z.; Xiao, P.; Zhang, Z.; Chen, X.; Li, X.; Zeng, Q.; Li, B.; Wu, Y.; Kang, M.; Zheng, J.; Wang, D.; Liao, Y. Engineered aggregation-induced emission luminogens-based framework with CO-releasing property for accelerating diabetic wound healing. *Chemical Engineering Journal* 2025, *524*, 168981. https://doi.org/10.1016/j.cej.2025.168981

13. Lu, J. Y.; Bu, Z. Q.; Lei, Y. Q.; Wang, D.; He, B.; Wang, J.; Huang, W. T. Facile microwave-assisted synthesis of Sb_2O_3-CuO nanocomposites for catalytic degradation of p-nitrophenol. *Journal of Molecular Liquids* 2024, *409*, 125503. https://doi.org/10.1016/j.molliq.2024.125503

14. Cazelles, R.; Drone, J.; Fajula, F.; Ersen, O.; Moldovan, S.; Galarneau, A. Reduction of CO_2 to methanol by a polyenzymatic system encapsulated in phospholipids-silica nanocapsules. *New Journal of Chemistry* 2013, *37*(11), 3721–3730. https://doi.org/10.1039/C3NJ00688C

15. Singh, R. K.; Singh, R.; Sivakumar, D.; Kondaveeti, S.; Kim, T.; Li, J.; Sung, B. H.; Cho, B.-K.; Kim, D. R.; Kim, S. C.; others. Insights into cell-free conversion of CO_2 to chemicals by a multienzyme cascade reaction. *ACS Catalysis* 2018, *8*(12), 11085–11093. https://doi.org/10.1021/acscatal.8b02646

16. Hollmann, F.; Witholt, B.; Schmid, A. [Cp* Rh (Bpy)(H2O)] 2+: A versatile tool for efficient and non-enzymatic regeneration of nicotinamide and flavin coenzymes. *Journal of Molecular Catalysis B: Enzymatic* 2002, *19–20*, 167. https://doi.org/10.1016/S1381-1177(02)00164-9

17. Lee, S. H.; Nam, D. H.; Park, C. B. Screening xanthene dyes for visible light-driven nicotinamide adenine dinucleotide regeneration and photoenzymatic synthesis. *Advanced Synthesis & Catalysis* 2009, *351*(16), 2589–2594. https://doi.org/10.1002/adsc.200900547

18. Lee, S. H.; Nam, D. H.; Kim, J. H.; Baeg, J.-O.; Park, C. B. Eosin Y-sensitized artificial photosynthesis by highly efficient visible-light-driven regeneration of nicotinamide cofactor. *ChemBioChem* 2009, *10*(10), 1621–1624. https://doi.org/10.1002/cbic.200900156

19. Lee, J. S.; Lee, S. H.; Kim, J.; Park, C. B. Graphene-Rh-complex hydrogels for boosting redox biocatalysis. *Journal of Materials Chemistry A* 2013, *1*(4), 1040–1044. https://doi.org/10.1039/C2TA00358A

20. Chenault, H. K.; Whitesides, G. M. Regeneration of nicotinamide cofactors for use in organic synthesis. *Applied Biochemistry and Biotechnology* 1987, *14*(2), 147–197. https://doi.org/10.1007/BF02798431

21. Zhao, H.; Van Der Donk, W. A. Regeneration of cofactors for use in biocatalysis. *Current Opinion in Biotechnology* 2003, *14*(6), 583–589. https://doi.org/10.1016/j.copbio.2003.09.007

22. Liu, W.; Wang, P. Cofactor regeneration for sustainable enzymatic biosynthesis. *Biotechnology Advances* 2007, *25*(4), 369–384. https://doi.org/10.1016/j.biotechadv.2007.03.002

23. Steckhan, E.; Herrmann, S.; Ruppert, R.; Dietz, E.; Frede, M.; Spika, E. Analytical study of a series of substituted (2,2′-bipyridyl)(pentamethylcyclopentadienyl) rhodium and iridium complexes with regard to their effectiveness as redox catalysts for the indirect electrochemical and chemical reduction of NAD(P)+. *Organometallics* 1991, *10*(5), 1568–1577. https://doi.org/10.1021/om00051a056

24. Vuorilehto, K.; Lütz, S.; Wandrey, C. Indirect electrochemical reduction of nicotinamide coenzymes. *Bioelectrochemistry* 2004, *65*(1), 1–7. https://doi.org/10.1016/j.bioelechem.2004.05.006

25. Bayan, R.; Karak, N. Bio-based hyperbranched polymer-supported oxygeneous graphitic-carbon nitride dot as heterogeneous metal-free solar light photocatalyst for oxidation and reduction reactions. *Applied Surface Science* 2020, *514*, 145909. https://doi.org/10.1016/j.apsusc.2020.145909

26. Zhu, J.; Xiao, P.; Li, H.; Carabineiro, S. A. C. Graphitic carbon nitride: Synthesis, properties, and applications in catalysis. *ACS Applied Materials & Interfaces* 2014, *6*(19), 16449–16465. https://doi.org/10.1021/am502925j

27. Magar, M. H.; Adole, V. A.; Waghchaure, R. H.; Pawar, T. B. Efficient photocatalytic degradation of eosin blue dye and antibacterial study using nanostructured zinc oxide and nickel modified zinc oxide. *Results in Chemistry* 2022, *4*, 100537. https://doi.org/10.1016/j.rechem.2022.100537

28. Chakravorty, A.; Roy, S. A review of photocatalysis, basic principles, processes, and materials. *Sustainable Chemistry for the Environment* 2024, *8*, 100155. https://doi.org/10.1016/j.scenv.2024.100155

29. Wang, X.; Wang, F.; Sang, Y.; Liu, H. Full-spectrum solar-light-activated photocatalysts for light-chemical energy conversion. *Advanced Energy Materials* 2017, *7*(23), 1700473. https://doi.org/10.1002/aenm.201700473

30. Ran, C.-K.; Niu, Y.-N.; Song, L.; Wei, M.-K.; Cao, Y.-F.; Luo, S.-P.; Yu, Y.-M.; Liao, L.-L.; Yu, D.-G. Visible-light photoredox-catalyzed carboxylation of activated C(sp^3)-O bonds with CO_2. *ACS Catalysis* 2021, *12*(1), 18–24. https://doi.org/10.1021/acscatal.1c04921

31. Gautam, H.; Yadav, R. K.; Mishra, S.; Shahin, R.; Singh, S.; Singhal, R.; Gupta, N. K.; Baeg, J. O.; Singh, A. P.; El-Hiti, G. A.; others. Crafting in situ boron and selenium-doped carbon nitride nanosheets for turbocharged benzaldehyde to benzyl alcohol under solar spectrum. *Diamond and Related Materials* 2024, *146*, 111140. https://doi.org/10.1016/j.diamond.2024.111140

32. Wu, H.; Huo, Y. One-step synthesis of efficient photocatalysts by TCAP-doped g-C_3N_4 for enhanced visible-light photocatalytic activity. *New Journal of Chemistry* 2020, *44*(3), 1127–1137. https://doi.org/10.1039/C9NJ05270D

33. Dutta Chowdhury, A.; Doong, R. Highly sensitive and selective detection of nanomolar ferric ions using dopamine-functionalized graphene quantum dots. *ACS Applied Materials & Interfaces* 2016, *8*(32), 21002–21010. https://doi.org/10.1021/acsami.6b06266

34. Mishra, S.; Yadav, R. K.; Mishra, D. K.; Kumar, K.; Gupta, N. K.; Singh, K.; Gothwal, S.; Baeg, J.-O. Metal-free functionalized carbon nitride as a photocatalyst driven by sunlight for acetal synthesis and selective regeneration of NAD(P)H cofactor. *Photochemistry & Photobiology* 2025, *101*(2), 471–482. https://doi.org/10.1111/php.14011

35. Zheng, H.; Huang, Z.; Wei, P.; Lin, Y.; Cao, Y.; Zhang, X.; Zhou, B.; Peng, C. Rh-functionalized imino-pyridine covalent organic framework assembled on $Ti_3C_2T_x$ (MXene) for efficient NADH regeneration and photoenzymatic

CO_2 reduction. *ACS Sustainable Chemistry & Engineering* 2025, 13(10), 4078-4092. https://doi.org/10.1021/acssuschemeng.4c10134

36. Yadav, R. K.; Baeg, J.-O.; Kumar, A.; Kong, K.; Oh, G. H.; Park, N.-J. Graphene-BODIPY as a photocatalyst in the photocatalytic-biocatalytic coupled system for solar fuel production from CO_2. *Journal of Materials Chemistry A* 2014, *2*(14), 5068–5076. https://doi.org/10.1039/C3TA14442A

37. Chaurasia, N.; Yadav, R. K.; Mishra, S.; Shahin, R.; Singh, S.; Gupta, N. K.; Pandey, S. K.; Yadav, M. K.; Baeg, J.-O.; Obaidullah, A. J. Shining bright: B@S-codoped graphitic carbon nitride nanorods illuminate enhanced catalytic C-N bond formation under visible-light. *FlatChem* 2024, *46*, 100669. https://doi.org/10.1016/j.flatc.2024.100669

38. Zhang, F.; Shi, F.; Ma, W.; Gao, F.; Jiao, Y.; Li, H.; Wang, J.; Shan, X.; Lu, X.; Meng, S. Controlling adsorption structure of eosin Y dye on nanocrystalline TiO_2 films for improved photovoltaic performances. *The Journal of Physical Chemistry C* 2013, *117*(28), 14659–14666. https://doi.org/10.1021/jp404439p

39. Jing, L.; Wang, D.; Xu, Y.; Xie, M.; Yan, J.; He, M.; Song, Z.; Xu, H.; Li, H. Porous defective carbon nitride obtained by a universal method for photocatalytic hydrogen production from water splitting. *Journal of Colloid and Interface Science* 2020, *566*, 171–182. https://doi.org/10.1016/j.jcis.2020.01.044

40. Srivastava, G.; Yadav, R. K.; Shahin, R.; Mishra, S.; Yadav, A. N.; Yadav, S. S.; Kumari, I.; Singh, K.; Baeg, J. O.; Gupta, N. K. Photocatalytic C-H activation for C-N/C-S bond formation over highly efficient solar light active supramolecular network organogels. *Journal of Sol-Gel Science and Technology* 2024, 111, 144–155. https://doi.org/10.1007/s10971-024-06410-z

41. Thaweesak, S.; Wang, S.; Lyu, M.; Xiao, M.; Peerakiatkhajohn, P.; Wang, L. Boron-doped graphitic carbon nitride nanosheets for enhanced visible light photocatalytic water splitting. *Dalton Transactions* 2017, *46*(32), 10714–10720. https://doi.org/10.1039/C7DT00933J

42. Liu, E.; Jin, C.; Xu, C.; Fan, J.; Hu, X. Facile strategy to fabricate $Ni_2P/g\text{-}C_3N_4$ heterojunction with excellent photocatalytic hydrogen evolution activity. *International Journal of Hydrogen Energy* 2018, *43*(46), 21355–21364. https://doi.org/10.1016/j.ijhydene.2018.09.195

43. Monga, D.; Basu, S. Tuning the photocatalytic/electrocatalytic properties of $MoS_2/MoSe_2$ heterostructures by varying the weight ratios for enhanced wastewater treatment and hydrogen production. *RSC Advances* 2021, *11*(37), 22585–22597. https://doi.org/10.1039/D1RA01760H

44. Singh, M.; Yadav, R. K.; Mishra, S.; Shahin, R.; Singh, S.; Singhal, R.; Gupta, N. K.; Baeg, J. O.; El-Hiti, G. A.; Kumar Yadav, K. Synthesis of a TBA-based polymeric photocatalyst for boosting the selective bio-reduction of furfural under solar light illumination. *ChemistrySelect* 2024, *9*(37), e202400732. https://doi.org/10.1002/slct.202400732

45. Chander, V.; Tewari, D.; Negi, V.; Singh, R.; Upadhyaya, K.; Aleya, L. Structural characterization of Himalayan black rock salt by SEM, XRD, and *in-vitro* antioxidant activity. *Science of The Total Environment* 2020, *748*, 141269. https://doi.org/10.1016/j.scitotenv.2020.141269